AMR-XAI-DWT: Age-Related Macular Regenerated Classification using X-AI with Dual Tree CWT

Naresh Kumar[*1], Gunikhan Sonowal [2], V. Balaji[3]

[1] Computer Science, Department of Mathematical and Physical Sciences, College of Arts and Sciences, University of Nizwa, Oman
[2] Faculty of Computer Technology, Assam Down Town University, Guwahati, India
[3] Department of Computer Science and Engineeing, School of Technology, GITAM University, Bengaluru, India
Emails: naresh@unizwa.edu.om; gunikhan.sonowal@gmail.com; balajipucs@gmail.com

Abstract

Age-related macular degeneration (AMD) is the leading cause of permanent vision loss, and drusen is an early clinical sign in the progression of AMD. Early detection is key since that's when treatment is most effective. The eyes of someone with AMD need to be checked often. Ophthalmologists may detect illness by looking at a color picture of the fundus taken using a fundus camera. Ophthalmologists need a system to help them diagnose illness since the global elderly population is growing rapidly and there are not enough specialists to go around. Since drusen vary in size, form, degree of convergence, and texture, it is challenging to detect and locate them in a color retinal picture. Therefore, it is difficult to develop a Modified Continual Learning (MCL) classifier for identifying drusen. To begin, we use X-AI (Explainable Artificial Intelligence) in tandem with one of the Dual Tree Complex Wavelet Transform models to create captions summarizing the symptoms of the retinal pictures throughout all of the different stages of diabetic retinopathy. An Adaptive Neuro Fuzzy Inference System (ANFIS) is constructed using all nine of the pre-trained modules. The nine image caption models are evaluated using a variety of metrics to determine their relative strengths and weaknesses. After compiling the data and comparing it to many existing models, the best photo captioning model is selected. A graphical user interface was also made available for rapid analysis and data screening in bulk. The results demonstrated the system's potential to aid ophthalmologists in the early detection of ARMD symptoms and the severity level in a shorter amount of time.

Keywords: Multiscale characteristics (MSC); Modified Continual Learning (MCL); Dual Tree Complex Wavelet Transform (DTCWT); Adaptive Neuro Fuzzy Inference System (ANFIS).

1. Introduction

Computer aided diagnosis (CAD) is becoming more popular in the field of medicine because of how well it can spot abnormalities brought on by a wide range of diseases. Because of how quickly they can be implemented, computer-aided design-based solutions are also useful in the healthcare sector. Another reason for their popularity is the dependability of CAD [1] systems. People are interested in CAD technology and their potential medical applications in particular at the moment.

In order to develop a CAD system, this proposed study discusses techniques for recognizing and labelling retinal abnormalities. The foundations of both image processing and machine learning may be found in these techniques. This investigation takes into consideration potential causes of retinal abnormalities, including diabetes-related retinopathy (DR) and age-related macular degeneration (AMD) [2]. If untreated, the aforementioned diseases are among the primary causes of permanent vision loss, according to ophthalmologists. Many illnesses have subtle early signs that may not be obvious to the naked eye.

The suggested work introduces an algorithm that relies heavily on the analysis of images. In order to automate the process of spotting problems in retina pictures with DR and AMD, many image processing methods are used.

Doi: https://doi.org/10.54216/FPA.150202
Received: July 20, 2023 Revised: November 19, 2023 Accepted: March 12, 2024

Image segmentation is very important here. In this research, we use a database of retinal images to evaluate the performance of several picture segmentation methods. The second major component of this method is machine learning [3]. Retinal pictures undergo a variety of image processing techniques before being analyzed. Using the out-of-the-ordinary things found, we compile a set of crucial characteristics whose values we next examine. The collection of feature vectors is split into a training set and an evaluation set. Here, we compare the performance of several machine learning approaches. Methods for identifying abnormalities in retinal images due to DR and AMD are presented in this proposal. The development of the algorithm is informed by interviews with ophthalmologists [4] and a review of the relevant literature. The unique contributions of this research are in the domains of image processing and feature selection, which are used to spot out-of-the-ordinary items. The proposed method may be useful for the early diagnosis of symptoms in patients with DR and AMD.

The researchers hope these findings will improve the speed and accuracy with which DR and AMD-related retinal abnormalities are diagnosed in patients. This study lays the groundwork for incorporating automated retinal flaw identification into a computer-aided design (CAD) system. The CAD system's high precision and user-friendliness make it superior to manual identification when it comes to detecting and classifying lesions in retina images [5]. The proposed method may reduce the amount of effort required by an ophthalmologist. The input pictures of the retina undergo a series of image processing steps designed to spot irregularities. A collection of feature values is compared to examine the newly found lesions. After lesions are found using image processing, they are classified using machine learning. Manual identification may be inaccurate since the human eye can't distinguish between minor color changes. Perhaps the time-consuming nature of anomaly identification from the retina image contributed to the decreased accuracy. The diagnostic value of a retinal picture may be diminished by a number of variables. To address such difficulties, the proposed strategy might be implemented. The proposed method has the potential to improve the speed and accuracy with which eye specialists diagnose and classify retinal disorders. These data sets feature retinal images captured at varying degrees of DR. There is a matching reality to each photo in the collection. Retinal images that are free of damage are also captured. Images of AMD-affected retinas may be seen online. The numerous abnormalities necessitate many visits to ophthalmologists [6]. According to medical recommendations, lesions are given certain features. To further narrow down on the specifics of the lesions of interest, a literature search was performed. The research was improved after taking into account the doctors' thoughtful feedback and suggestions. Since this research was overseen by seasoned eye professionals, we think the recommended technique may be useful for retina physicians in their regular work.

The primary objective of this work is to produce symptom captions for classification purposes, after pre-processing Optical Coherence Tomography (OCT) [7] pictures and retinal fundus images, for three eye illnesses and four severity levels of DR. Feature extraction is a core component of several popular automated computer-assisted screening systems used for caption generation and disease classification. Eye diseases are classified into different severity groups, and symptomatic descriptions for retinal fundus and OCT pictures are created. Finding a computer-aided, deep learning-based system for diagnosis and classification to assist the ophthalmologist in avoiding blindness among the vast number of people across the world who suffers from different eye illnesses is the major objective of this research. The main objective is to utilize the deep learning-based system's generated captions to detect and categories retinal fundus pictures into different degrees of diabetic retinopathy.

An overview of the research is as follows: Section 2 provides a review of the relevant literature, Section 3 details the methodology to be used, Section 4 discusses the experimental results and analysis, and Section 5 offers a summary and suggestions for future research.

2. Related Work

Age-related macular degeneration is theorized to be caused by the creation of Type IV collagen, which thickens Bruch's membrane and choriocapillaris septa after chronic, low-level exposure to reactive oxygen in the choriocapillaris endothelium (ARMD). Reduced blood supply to the retina has been hypothesized to have a role in the onset of ARMD and the growth of drusen [8]. Research in animals has resulted in models of chronic, low-level photosensitizing injury to the choriocapillaris [9]. In a mouse model of protoporphyria, a 10-fold increase in protoporphyrin IX and exposure to blue light (380-430 nm, 14W/cm2) led to a time- and light-dependent increase in choriocapillaris and subretinal RPE basal laminar like deposits. Protoporphyrin mice, when exposed to blue light for seven months, had a Bruch's membrane that was much thicker than that of control mice. There was a complete basement membrane-to-endothelium thickening in the choriocapillaris.

The retinal pigment epithelium (RPE) and rod outer segments of both the experimental animals and the light and dark controls showed no signs of light-induced degeneration or other abnormalities. The POLA experiment found no association between sun exposure and either pigmentary changes or ARMD [10]. Early age-related macular degeneration was more likely to occur in those who spent more than five hours a day in the summer sun

Doi: https://doi.org/10.54216/FPA.150202
Received: July 20, 2023 Revised: November 19, 2023 Accepted: March 12, 2024

throughout adolescence, between the ages of 16 and 30, and at the time of the initial test (RR, 2.20, 95 percent CI: 1.02 to 4.73). Putting on a hat and sunglasses also helped shield your eyes from the sun. In order to collect information for the Blue Mountains Eye Study, standardized questionnaires were used (Pham et al., 2009). There was no link established between sun exposure and ARMD risk. In the European eye research (EUREYE study), those with low antioxidant levels were more vulnerable to inadequate levels of protection against blue light, increasing their risk for ARMD ([11].

The diagnosis of AMD has been the subject of several academic papers. Twenty normal-appearing OCT pictures and fifteen images with AMD make up the duke SD-OCT dataset [12]. This was achieved by using a Histogram of Oriented Gradient (HOG) descriptor across many scales throughout the feature extraction procedure. The characteristics were then labelled using a support vector machine classifier with leave-3-out cross-validation. Diseased volumes were defined as those in which anomalies comprised 33% or more of the total number of pictures inside the volume. This approach has an overall accuracy of 93.3%. By calculating the Estimated Line value of RPE, [13] used the Gaussian filter to reduce noise in the photos and then extracted the RPE layer (EL-RPE). To eliminate the RNFL, they used the duke SD-OCT dataset in conjunction with ELRPE and a New Estimated line of RPE (NERPE) [14]. The main problem with this method was that it did not work on pictures that had a lot of background noise. Bruch's Membrane (BM), Inner Limiting Membrane (ILM), and RPE layers were initially proposed for semi-automatic segmentation in [15]. The attributes were gathered manually. We were able to differentiate between AMD and healthy images using leave-1-out cross-validation and linear regression. Area Under Curve (AUC) analysis was used to measure the system's efficiency, and a value of 0.99 was found. The study was performed using Bioptigen SD-OCT images. Manual corrections and accurate retinal layer segmentation were required to reduce the likelihood of drawing incorrect findings. Using the duke dataset, [16] studied how well it could distinguish between photos with AMD and normal eyes. The RPE layer was singled out using a thresholding technique depending on intensity. By applying a curve approach to refine the layer, a 96 percent precision was attained. The pervasive drusen was the major issue with this method since it led to an erroneous baseline. The researchers also only used a small portion of the whole dataset. Using a correlation-based feature subset selection strategy is recommended for feature extraction from OCT images in [17]. Sequential Minimal Optimization (SMO) was used to create categories for the photographs. Using the Duke dataset, a reported accuracy of 96.6% was found. To create the spatial pyramid, the OCT image was first rescaled using the Multi-Scale Spatial Pyramid (MSSP) technique. Researched by [18], who used the Duke Dataset. They extracted the ROI from the 512256 pictures. Then, kernel regression was used to eliminate the speckle noise in the images. To uncover the RPE layer behind the RNFL, we used intensity-based thresholding to selectively eliminate the RNFL layers from the denoised image.

Polynomial fitting was used to get the best possible t-line. Sensitivity was just 0.56, while overall accuracy was 92%. Using a CNN model, [19] was able to label images as having AMD or normal. Using Google Net for transfer learning, as was recommended, improved accuracy on the duke dataset to 94%. The approach in [20] used a modified version of the VGG-16 CNN model to categories the Heidelberg Spectral is dataset. The network, which consisted of twenty-one nodes, was 93.4 percent accurate. In [21]'s suggested method for learning a vocabulary, images were scaled to one of three different levels.

Using techniques like Scale-Invariant Feature Transform (SIFT), features were assessed at individual patches and their sparse representations were then joined together to generate the global representation. On the duke dataset, 96.6 percent accuracy was achieved when the input images were identified using the linear SVM as the classier. There were 37206 cases of Wet AMD, 8616 cases of dry AMD, 51140 cases of 8 normal pictures, and 750 test images used in [22]. A transfer learning model was trained and tested using the OCT pictures, and it attained an overall accuracy of 96.53 percent. In [23], a novel AlexNet was trained to serve as the basis for a deep network. Using the Mendeley dataset [24], the network's accuracy was calculated to be 98.26%. The researchers in [25] employed a 3D segmentation strategy for their SD-OCT analysis. Drusen volume, HIS volume, and the curvature of the MZ-EZ boundary were the three parameters collected. EEG signal effectively used to address the autism disorder detection problem [25]. The duke dataset was used with an RF classifier that obtained 97% accuracy. One significant limitation of our research was its inability to detect life-threatening conditions in cases when retinal layer segmentation had failed.

2.1 Outlined research issues

In this section, we will describe the main drawbacks of the existing methods for detecting AMD that have been reported. Due to a large difference between the calculated and true baseline, the statistical methods utilized to identify dry AMD exhibited a poor sensitivity. The computational complexity was increased by the large number of learnable parameters in the network, and much of the deep learning work was done via transfer learning methods. To train and test, prior deep learning methods often used data from the same OCT machine, restricting their versatility.

Doi: https://doi.org/10.54216/FPA.150202
Received: July 20, 2023 Revised: November 19, 2023 Accepted: March 12, 2024

3. Proposed Methodology

The diagnostic technique relies on the statistical classification of vision-threatening lesions in the retina, pinpointing the macula area is crucial. The macula, also known as the macula lutea, is a 5.5 mm by 5.2 mm area of the retina that follows the direction of the large passing arcades. The macula, a specialized region of the eye responsible for sharp, centre vision, deteriorates gradually in those with age-related macular degeneration. When drusen are tiny, the patient may not notice anything out of the ordinary, but they may cause significant vision loss if ignored, especially if they are in the macula. Therefore, for automated diagnosis of abnormalities and their severity, it is crucial to identify and label the macular area in a retinal picture. As a solution, we zeroed down on the macula region, which is posterior to the OD and is surrounded by the temporal superior and inferior vascular arcades, as the area of interest (ROI) that contains all relevant anatomy. Due to the edge colour fluctuation in fundus images, ROI recognition is one of the most significant and difficult problems in medical image processing. In a colour retinal picture, the macula stands out as a darker region due to its location in the central depression of the retina. The specifics of the five different freely available SD-OCT datasets used in the proposed methods are shown in Table 1.

3.1 Dataset description

Archive at Duke The collection includes photographs taken of healthy individuals as well as those with AMD and DME. There were fifteen sets of photographs for every imaginable category. The Spectral is SD-OCT was used to get the OCT data from Duke, Harvard, and the University of Michigan. There was just the dry AMD set of statistics to choose from. The suggested investigation used thirty image volumes, fifteen from the dry AMD group and fifteen from the normal group.mFrom the SD-OCT NOOR data collection Fifty normal OCTs, forty-eight OCTs of dry AMD, and fifty OCTs of DME were provided by Tehran's Noor Eye Hospital. The scan size for this dataset was 89 74mm2, and the axial resolution was 35m, however the lateral and azimuthal resolutions varied amongst individuals. The Researchers at [21] gathered 108,310 pictures from 4,686 people: 37,205 with wet AMD; 11,349 with DME; 8,616 with dry AMD; and 51,140 normal. The proposed method was tested on both normal and picture types indicative of dry and wet AMD.
A total of 107 cases of diabetic retinopathy and 30 cases of central serous retinopathy were included in the dataset supplied by [22]. Information was gathered using a Cirrus HD-OCT instrument at the Sankara Nethra Laya Eye Hospital in Chennai, India. Degeneration of the macula due to ageing is known as age-related macular degeneration (AMD). Among those over the age of 45, its prevalence is much greater than that of diabetic retinopathy. Genetics, a persistent photo-destructive impact, and nutritional problem are only some of the unknowns that contribute to our incomplete understanding of AMD's etiology. Dry AMD and Wet AMD are the two main types of the disease. Nonexudative AMD, often known as dry AMD, is not a neovascular condition. Retinal pigment epithelium atrophy is a hallmark of this condition (RPE). Drusen and a broad region of atrophy were detectable by ophthalmoscopy in the advanced stage. Active neovascularization beneath the RPE leads to exudation, hemorrhage, and scarring in wet age-related macular degeneration (AMD), also known as neovascular or exudative AMD. If left untreated, this condition would damage the photoreceptors irreparably and result in fast vision loss.

Table 1: Datasets Used in Macular Regeneration

Datasets Used in Macular Regeneration	Category	No. of images
Duke (30 subjects (2 classes: AMD and Normal))[16]	Normal	15
	AMD	15
SD-OCT Noor (98 subjects (50 normal, 48 dry AMD)) [17]	Normal	50
	AMD	48
Bioptigen SD-OCT (384 subjects (2 classes: AMD and Control)) [18]	Normal	115
	AMD	269

Doi: https://doi.org/10.54216/FPA.150202
Received: July 20, 2023 Revised: November 19, 2023 Accepted: March 12, 2024

Mendeley (96961 images (2 classes: AMD and Normal)) [19]	Normal	51140
	AMD	45821
OCT-ID (261 images (2 classes: dry AMD and Normal)) [20]	Normal	206
	AMD	55

The therapy and prognosis of AMD greatly improve if the disease is caught early. One of the fundamental tests is a photograph of the fundus. Images from both AMD and non-AMD (myopia, normal control, etc.) eyes are included in the present collection. These images show the classic AMD symptoms like as drusen, exudation, haemorrhage, etc.

32. Classification

There are two phases to the grading procedure. The first step involves a pre-trained Convolutional Neural Network and Explainable AI. The second phase of the project is an Adaptive Neuro Fuzzy Inference System based on Modified Continual Learning (MCL) (ANFIS).

3.2.1 Explainable Artificial Intelligence with Dual Tree Complex Wavelet Transform (EAI-DTCWT)

For the purpose of generating explanations and stories, we suggest using an image-to-image transformer model. T5 is a pre-trained model that takes in text and returns text. It's a model of a transformer that has both an encoder and a decoder. To produce contextual embedding of the input text, each encoder block employs a multi-head attention layer. The T5 model differs most noticeably from the vanilla transformer by applying the layer normalizing layer before to the sub-layer (attention and fully connected layer). In addition, it employs a unique positional encoding method in contrast to the standard transformer. T5 is pre-trained on the Colossal Clean Crawled Corpus (C4) and is easily customizable for a wide range of downstream text-to-text activities. In addition, the pre-trained T5 model acts as a mentor to a more compact student NMT model that is optimized for the purpose of transitioning explanations into narratives.

This reduces the total number of model parameters, which speeds up the training process. We assume an encoder-decoder based student model to be trained using the common cross-entropy loss function in order to fine-tune the explanation-to-narrative generating model:

$$\iota_{\text{student}} = -\sum_{t=1}^{T} \log p(y_{t+1} \mid y_{1:t}, x) \qquad (1)$$

T is the story's final length, x is the input after being linearized, and y is the story's starting point. Our goal is to reduce the size of a pre-trained T5 teacher model that already has encoder and decoder layers by reducing the number of layers in the student model. We suggest a new method of knowledge distillation [149] that involves first transferring the expertise of a pre-trained teacher model to a novice model, and then refining that novice model with the use of a synthetic dataset. A pre-trained instructor is used as a model for the student to learn from, and the student is then fine-tuned using the dataset. The computational expense of re-fine-tuning the student model on a created dataset is avoided with this method.
In order to analyses signals effectively, one might make use of the complex wavelet transform, which is a well-organized instrument. Using an analytic filter, the Complex Wavelet Transform (CWT) separates the signal into its imaginary and real components. These coefficients help in making amplitude and phase estimations. The amplitude measures the strength of the singularity, whereas the phase pinpoints its location. Hilbert Transform (HT) is used to create the systematic or quadrature version of the picture. It is claimed that a complex signal is analytic if its imaginary portion is the Hilbert transform of its real part. Gabor initiated the use of Hilbert transform into the theory of signals [89]. For a real signal f (t) the complex signal x (t) is defined as:

$$x(t) = f(t) + jg(t) \qquad (2)$$

Where $g(t) = H\{f(t)\}$, Hilbert transform of $f(t), j = \sqrt{g(t)} - 1$. Multifaceted solutions are generated by applying the analytic formulation idea to the filter bank structure of traditional DWT. Once an appropriate design

Doi: https://doi.org/10.54216/FPA.150202
Received: July 20, 2023 Revised: November 19, 2023 Accepted: March 12, 2024

has been made, complex-valued filter coefficients may replace their real-valued counterparts. The complex filter is also decomposed into its component real-valued filters. The pair of Hilbert transformations is the impulse response of two filters with real values. DT-filter CWT's bank architecture may be thought of as two parallel typical DWT trees, one of which is a real tree and the other an imagined tree.

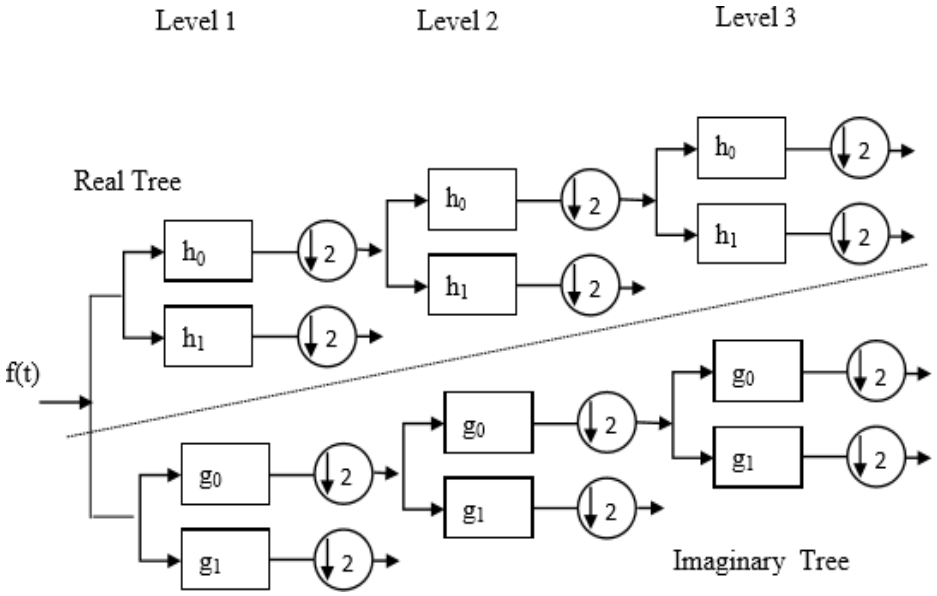

1 (a) Decomposition filter bank

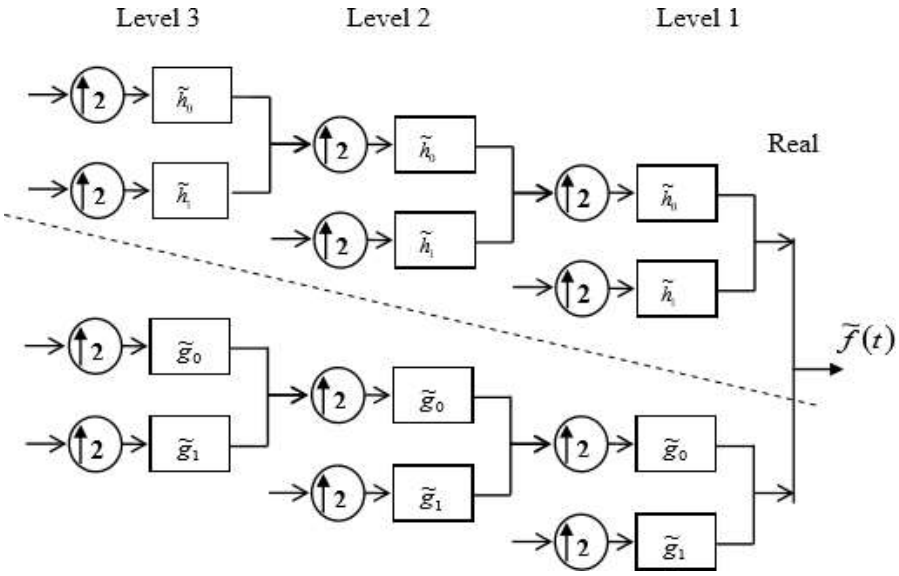

1 (b) Reconstruction filter bank

Figure 1: Filter bank Structure for 1-D DT-CWT

The 1D-DT-CWT uses complex filters, represented as $(h_x + \mathrm{j}g_x)$. Where h_x is the filter set $\{h_0, h_1\}$, and g_x is the filter set $\{g_0, g_1\}$. The h_0, h_1 are the real tree real-valued low-pass and high-pass filters and g_0, g_1 are the real-valued low-pass and high-pass filters for imaginary tree. The filter coefficients h_0 and h_1 are numerically different for primary and higher levels.

The synthesis filter pair illustrated in Figure 1(b) form bi-orthogonal or orthogonal pairs with the decomposition filter pairs as depicted in Figure 1(a). The 2D-DT-CWT structure is an extension of conjugate filtering in 2D

Doi: https://doi.org/10.54216/FPA.150202
Received: July 20, 2023 Revised: November 19, 2023 Accepted: March 12, 2024

case. The filter bank organization of 2D Dual-Tree is presented in Figure 1. For 2-D structure four trees for analysis and synthesis are needed. The conjugate filter pairs for 2dimensions are represented in equation-3.

$$(h_x + \mathrm{j}g_x)(h_y + \mathrm{j}g_y) = (h_x h_y - g_x g_y) + \mathrm{j}(h_x g_y + g_x h_y) \quad (3)$$

The ability to express a function at several scales is DWT's major strength. The expansion of a function as a wavelet series is

$$f(x) = \sum c_{j0}(k)\phi_{j_0,k}(x) + \sum\sum d_{j=j0}(k)\Psi_{j,k}(x) \quad (4)$$

where $j0$ is an arbitrary starting scale, $\psi(x)$ is the wavelet, $\phi(x)$ is the scaling function, $cj0(k)$ is the approximation coefficient and $dj(k)$ is the detail coefficient.

The design of DT-CWT comprises orthogonal wavelets to show up as Hilbert transform pair. The scaling filters of real and imaginary trees must be varied by a half sample. Let h_0, h_1 and g_0, g_1 correspond to two Conjugate Quadrature Filter (CQF) pair in the filter bank then

$$f_1(n) = -1^{(n-1)}h_0(1-n) \quad (5)$$

In Z-Transform

$$H_0(z)\boldsymbol{U}_0(z^{-1}) + \boldsymbol{H}_{\mathrm{g}}(-z)H_0(-z^{-1}) = 2$$
$$\boldsymbol{H_1}(z) = z^{-1}H_0(z^{-1}) \quad (6)$$

If $\psi_h(t)$ and $\psi_g(t)$ appeared Hilbert Transform pair, then

$$\psi_g(t) = \{\psi_h(t)\} \text{ and } \psi_g(\omega) = -j \cdot \mathrm{signum}(\omega)\,.\psi_h(\omega)$$
$$\left|\psi_g(\omega)\right| = |\psi_h(\omega)| \quad (7)$$

Here $\psi_g(\omega)$ and $\psi_h(\omega)$ are the Fourier Transforms of the wavelets $\psi_g(\mathrm{t})$ and $\psi_h(\mathrm{t})$ related to high pass filters of imaginary and real parts of DT-CWT. If $\boldsymbol{H}_{\mathbb{0}}(\omega)$ and $G_{\mathrm{J}}(\omega)$ are the Fourier Transforms of scaling filters h_0 and g_0, then the two low pass filters are associated as

$$|G_0(\omega)| = |H_0(\omega)| \text{ and } G_0(\omega) = H_0(\omega)e^{-j\theta(\omega)}$$
$$\theta(\omega) = \frac{\omega}{2} \text{ for } |\omega| < \mathrm{n} \quad (8)$$

Then the relation between the digital filter $g_{\ominus}(\mathrm{n})$ and $h_0(\mathrm{n})$, is a half-sample delay i.e.

$$g_0(\mathrm{n}) = h_0\left(\mathrm{n} - \frac{1}{2}\right) \quad (9)$$

Since the half sample delay filters cannot be realized with FIR filter, then the design of FIR filters $g_0(\mathrm{n})$ and h_0 is implemented by means of Grobler base. Selesnick DT-CWT uses orthogonal filter coefficients. First level and higher-level analysis Filter bank of DT-CWT uses different pair of dissimilar Hilbert wavelets. All the reconstruction filters are the time-reversed representation of their subsequent analysis filters.

Table 2: Pseudocode for XAI-DTCWT

Initialize cluster centroids $\mu_i, i = 1, \ldots, k$ randomly
{ Repeat
$\forall x^t$ in x
$c^t = 1$ if $\|x^t - \mu_i\| = \min\|x^t - \mu_j\|$, i and j }

Doi: https://doi.org/10.54216/FPA.150202
Received: July 20, 2023 Revised: November 19, 2023 Accepted: March 12, 2024

$c^t = 0$ otherwise i
$\forall \mu_i, i = 1, \dots, k$
$\mu_i = \sum_{i=1}^{m} t(C^t X^t) \Big/ \sum_{i=1}^{m} t(C^t)$
Until μ_i converge

where c^i is the i^{th} cluster and μ_i is the centroid of the cluster c_i. The goal of the proposed strategy is to employ a clustering technique known as MCL-ANFIS to automatically identify drusen and evaluate them without human supervision.

3.2.2 Modified Continual Learning (MCL) based Adaptive Neuro Fuzzy Inference System (ANFIS)

A fuzzy generalization exists for ANFIS clustering, called fuzzy c-means, or MCL. MCL was proposed initially. The essential change it makes to the ANFIS algorithm is in the determination and expression of pixels' class memberships, from Boolean membership to fuzzy; as a result, the calculation of class means has to be modified to incorporate each pixel's fuzzy MCL clustering allows a single region of an image to be in two or more clusters by assigning varying degree of membership to each pixel of an image.
Unlike ANFIS each data point in MCL may belong to more than one cluster center, they provide best result for overlapped data set. It acts on minimizing the objective function and starts with fuzzy pixel classification to segment an image.

Table 3: Pseudocode for ANFIS Clustering

Initialize the membership matrix; U=$\left\|u_{ij}\right\|$ matrix, $U^{(0)}$
{ For i= 1:N For j+1:C
(1) At k-step: calculate he centre vector $C^{(k)} = \|c_i\|$ matrix, with $U^{(k)}$ $C_j: C_j = \frac{\sum_{u_{jij}}^{\infty} x_i}{\sum m}$
(2) Update membership matrix u_{ij} with $U^{(k)}$ and $U^{(k+1)}$
end
end
}
while $\|U^{(k+1)} - U^{(k)}\| < \delta$ where δ is a termination criterion between [0,1] then stop otherwise, set $k = k + 1$ and go to (i)

$$J_m = \sum_{i=1}^{N} \sum_{j=1}^{C} \|x_i - c_j\|^2, 1 \le m \le \infty \qquad (10)$$

where m is any real number greater than 1 . Here N is the number of objects and C is the number of clusters, where u_{ij} is the degree of membership that the object x_j pertains to the cluster center $c_i, U = u_{ij}, i = 1,2, \dots, C, j = 1,2, \dots, N. C = c_i, i = 1,2, \dots, C$ is the cluster prototype matrix and c_i is the prototype of the center of cluster i. The pseudocode of the MCL-ANFIS algorithm is shown below. In Fig. 3, the transfer function of the secondary path from *y(n)* to *e(n)* is shown. The lag in the path is introduced due to the control components such as ADC, DAC, filters, etc. which causes instability as it disrupts the alignment of the reference and error

Doi: https://doi.org/10.54216/FPA.150202
Received: July 20, 2023 Revised: November 19, 2023 Accepted: March 12, 2024

signal. This instability raises the need to estimate secondary path transfer function *S(z)* as *Ŝ(z)*, which modifies the LMS algorithm to Filtered- reference- LMS (FxLMS) algorithm. The estimation of *Ŝ(z)* must be such that the phase error between *S(z)* and *Ŝ(z)* must not be greater than ±90º, otherwise, the stability of the algorithm cannot be guaranteed [8][9].

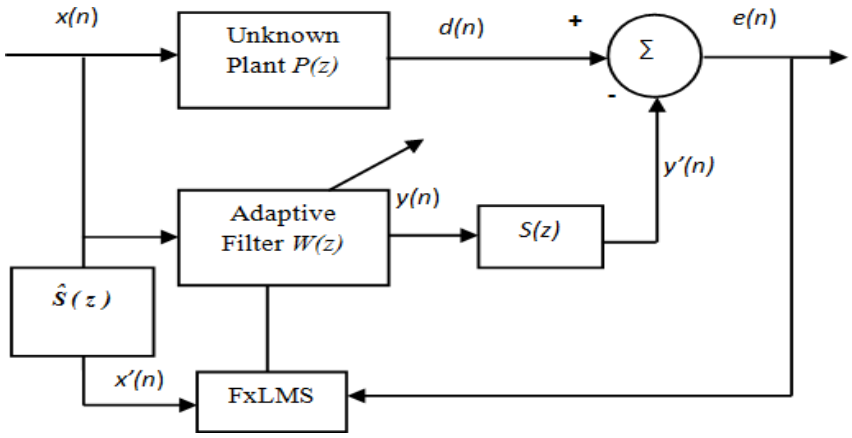

Figure 2: Block diagram of MCL WITH ANFIS

The control signal is derived at any time instant *'n'* by finite impulse response filtering, A Dataset is commonly sub-divided into Training and Testing Datasets. By convention, 80% of the Dataset is considered as Training Dataset and it is used for training purpose. The remaining 20% of the Dataset is considered as Testing Dataset and it is used for Testing purpose. Some of the most popular algorithms based on the Batch size are Batch Gradient Descent Algorithm, Stochastic Gradient Descent Algorithm and Mini Batch Gradient Descent Algorithms.

Training Batch size: Training Batch size is the number of samples of a training Dataset which are passed through a Deep Learning Model in a particular iteration.

Testing Batch size: Testing Batch size is the number of samples of a Testing Dataset that are passed through a Deep Learning Model in a specific iteration. Table 4 indicates a set of Hyper-Parameters which are kept constant during analysis.

Table 4: Hyper-Parameter Values and Settings

S.No	**Hyper-Parameters**	**Values**
1.	Learning Rate	10^{-}
2.	Drop-out rate	0.5
3.	Activation Function	Relu
4.	Number of Epochs	10
5.	Training Layers	Top-4 Layers

Doi: https://doi.org/10.54216/FPA.150202
Received: July 20, 2023 Revised: November 19, 2023 Accepted: March 12, 2024

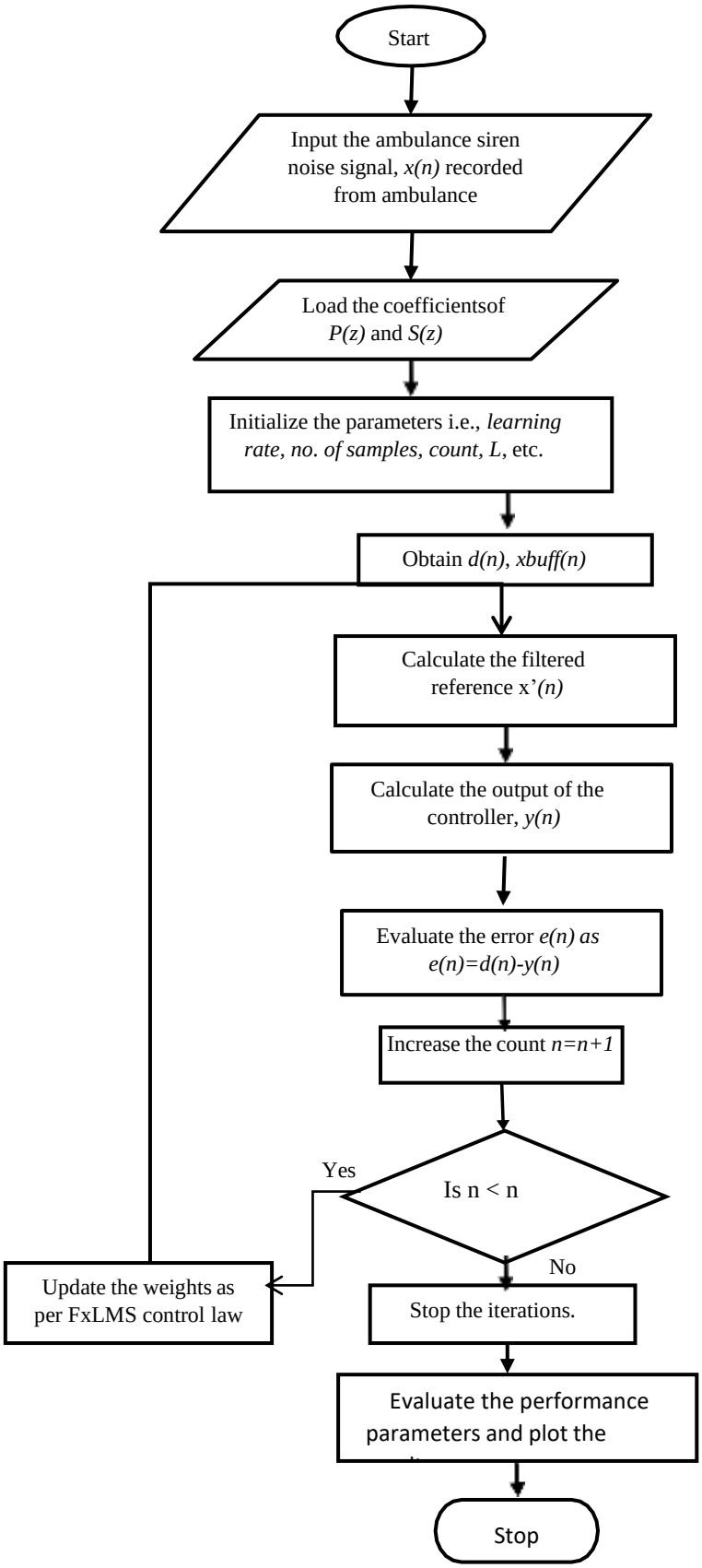

Figure 3: Block Diagram of MCL-ANFIS Algorithm

Doi: https://doi.org/10.54216/FPA.150202
Received: July 20, 2023 Revised: November 19, 2023 Accepted: March 12, 2024

Out of which, Learning-rate value is taken from the previous analysis and the rest of the Hyper-Parameters are freeze as per the literature. The entire work cycle is carried out in two sections. Part-I considers 02 . different Datasets Dataset-1 and Dataset-2 with various Batch sines which is training and testing Batch sizes as mentioned in Table 5. Fach Batch size combination is represented with a unique id namely Batch ID. The values of these Batch IDs considered are from A to O for Dataset-1 and A to D for Dataset-2. The accuracies at these different Batch sines were calculated through experimentation. Here, the InceptionV3 Model is considered for analysis purpose.

Table 5: Batch Size Details

Dataset	**Batch ID**	**TrBS**	**TES**
DATASET − I (150/40)	A	2	1
	B	4	1
	C	4	2
	D	15	6
	E	30	12
	F	40	11
	G	50	14
	H	60	15
	1	70	18
	J	80	21
	K	100	30
	L	120	33
	M	130	12
	N	140	36
	0	150	40
DATASET = 2 (443/92)	*A*	6	1
	B	12	3
	C	44	9

Doi: https://doi.org/10.54216/FPA.150202
Received: July 20, 2023 Revised: November 19, 2023 Accepted: March 12, 2024

	D	147	30

After AC training, we start MCL training. In this phase, only KB-RNN and others in the purple box are trainable. The trained binary task-based mask a_t is element-wise multiplied by the output vectors of KB-RNN. This operation protects those inaccessible units since no gradient flows acroes them while allowing those accessible units to be updated since the mask does not stop gradients for them. This clearly enables forward knowledge transfer because those accessible units selected by the mask represent the knowledge from the previous tasks that can be leveraged by the current/new task. It also enables backward knowledge transfer and avoidance of CF because (1) if the accessible units are not important to the previous tasks, any modification to them does not degrade the previous tasks' performance, and (2) if the accessible units are useful for some previous tasks, updating them enable them to improve as we now have more data to enhance the shared knowledge.

The confusion matrix was used to analyses the outcomes of the suggested works. That matrix has values of M, N, 0, and P for the proportions of True Positives (TP), False Negatives (FN), and False Positives (FP), respectively. It was found that TP and TN returned correctly categorized data whereas FP and FN returned incorrect findings. Classification performance was evaluated by four parameters: precision, F1-score, recall, and accuracy.

4 Experimental Results

The confusion matrix was used to analyses the outcomes of the suggested works. That matrix has values of M, N, 0, and P for the proportions of True Positives (TP), False Negatives (FN), and False Positives (FP), respectively. It was found that TP and TN returned correctly categorized data whereas FP and FN returned incorrect findings. Classification performance was evaluated by four parameters: precision, F1-score, recall, and accuracy.

$$\text{Accuracy} = \frac{P + M}{O + P + N + M} \tag{11}$$

The rate at which false positives occur is known as the False Positive Rate (FPR). The optimal FPR for a reliable classifier is zero.

$$FPR = \frac{O}{O+P} \tag{12}$$

The positive value of prediction is given by precision. This value provides details about how our system is effectively avoiding FPs. It is measured as,

$$\text{Precision} = \frac{M}{M + O} \tag{13}$$

Specificity is the measure of how well a test can identify true negative.

$$\text{Specificity} = \frac{P}{P + O} \tag{14}$$

Recall is also known as sensitivity gives information about how effectively the model decreases FN. This is measured as,

$$\text{Recall} = \frac{M}{M + N} \tag{15}$$

The Receiver Operating Characteristic (ROC) curve measures how well a system can detect while also minimizing false positives (ROC). With (1-Specificity) on the x-axis and sensitivity on the y-axis, Figure 3 shows a ROC curve for a variety of test values. A curve that is closer to the diagonal than the top and left boundaries indicate poor test accuracy.The area under the curve (AUC) is a universal measure of a test's ability to detect the presence or absence of a condition. The AUC may take on any value between 0 and 1, inclusive. The best classifier has an AUC of 1, whereas random performance has an AUC of 0.5.
Drusen towards the periphery are poorly illuminated and so difficult to see. We pre-processed the OD-removed image using a CLAHE and a homomorphic filter to boost contrast and fine- tune illumination. After the image has been preprocessed, DWT is used to normalize the results.The drusen along the fundus's edges were clearly

Doi: https://doi.org/10.54216/FPA.150202
Received: July 20, 2023 Revised: November 19, 2023 Accepted: March 12, 2024

visible once the image was normalized. Figure 3 displays the approximation coefficient of a wavelet-transformed image, which is rather large.
DWT increases the resolution of the approximation sub band that is taken into consideration inlater processing by decreasing the transform coefficients at lower scales. Clustering on the approximation channel is then used to assign drusen, background, or blood vessel status to thevarious parts of the retinal image.
The density of drusen tends to peak early in a cluster then gradually fade as it progresses. Environment typical of the Drusen the Receiver Operating Characteristic (ROC) curve measures how well a system can detect while also minimizing falsepositives (ROC). ROC curves for different test values are shown in Figure 3, where (1-Specificity) is shown on the x-axis and sensitivity is shown on the y-axis. A curve that is closerto the diagonal than the top and left boundaries indicate poor test accuracy.
The area under the curve (AUC) is a universal measure of a test's ability to detect the presenceor absence of a condition. The AUC may take on any value between 0 and 1, inclusive. The best classifier has an AUC of 1, whereas random performance has an AUC of 0.5.
Drusen towards the periphery are poorly illuminated and so difficult to see. We pre-processedthe OD-removed image using a CLAHE and a homomorphic filter to boost contrast and fine- tune illumination. After the image has been preprocessed, DWT is used to normalize the results.
DWT increases the resolution of the approximation sub band that is taken into consideration inlater processing by decreasing the transform coefficients at lower scales. Clustering on the approximation channel is then used to assign drusen, background, or blood vessel status to thevarious parts of the retinal image. The density of drusen tends to peak early in a cluster then gradually fade as it progresses.
Figure 4 displays the clusters obtained using MCL classification. The MCL clustering technique was used, which assigned a membership score to each pixel. The sizes of the clustersvaried from 3 to 12. The image was under-segmented when 12 clusters were used, whereas it was over-segmented when just three were used. After some trial and error, we discovered thateight clusters worked well. The brightest drusen are often found in the latter two classes; identifying them accurately can help pinpoint their respective regions.

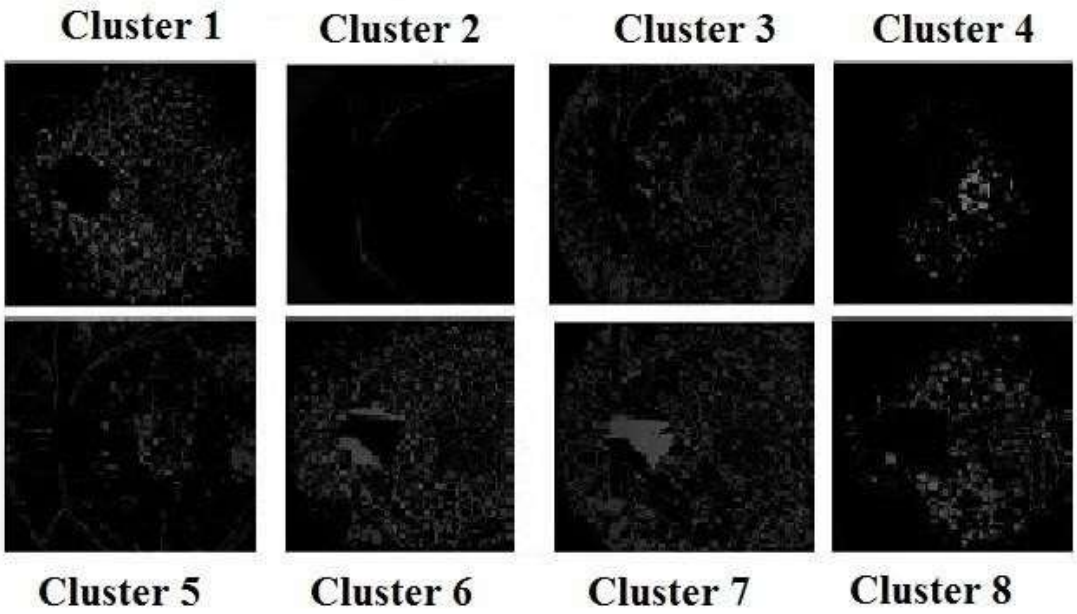

Figure 4: Retinal Image in 8 Clusters with Drusen Detected Image Using ANFIS and MCL Clustering Techniques.

Drusen identification in the most recent two clusters was improved by mapping the intensity to a new range. Therefore, the contrast of the segmented picture is automatically increased. The morphological operator was employed to fuse the disparate globs into one. Segmented drusen had their signal strength increased and identities confirmed by using the connected component properties. Each pixel in the image that represented a drusen was given the same name, while all other pixels were given the value 0. MCL-ANFIS processing, with k ranging from 3 to 12, was first applied to the enhanced image in order to isolate the drusen region. ANFIS and MCL clustering algorithms were usedto uncover the image displayed in Figure 5, in which large AMD were emphasized in red, medium AMD in green, and microscopic AMD in blue.

Doi: https://doi.org/10.54216/FPA.150202
Received: July 20, 2023 Revised: November 19, 2023 Accepted: March 12, 2024

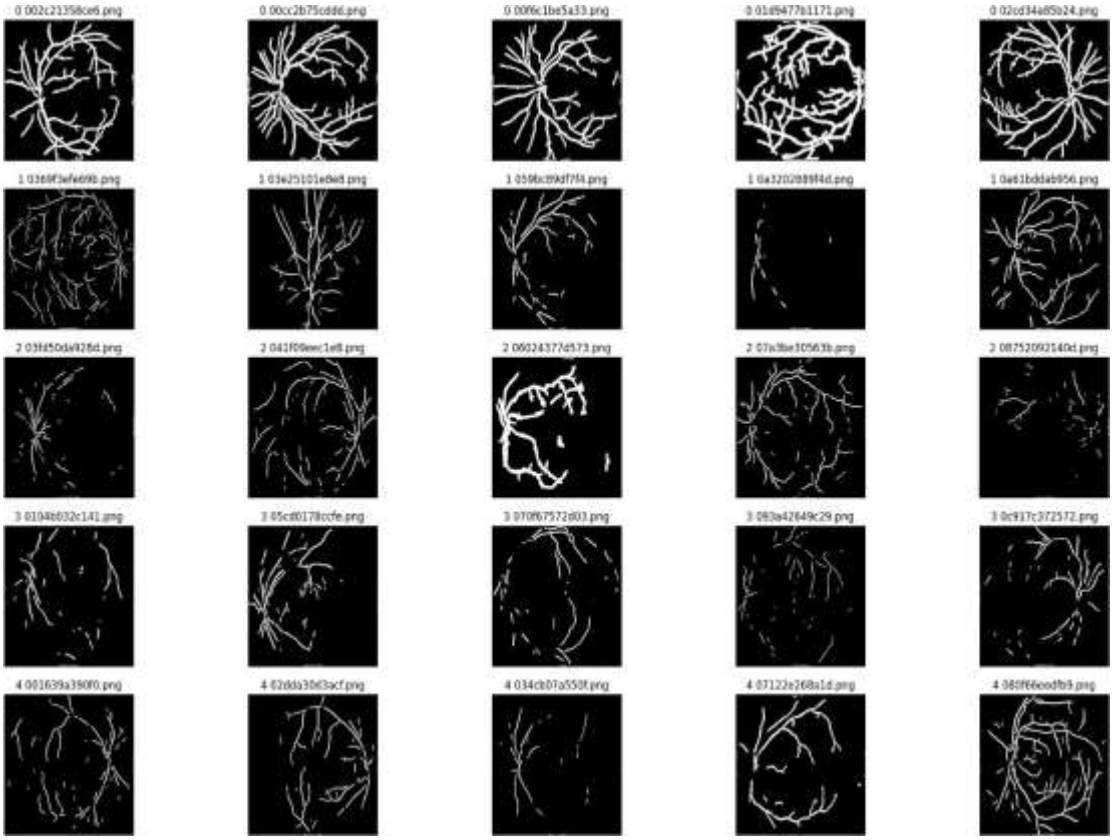

Figure 5: Drusen Detected Image Using ANFIS and MCL Clustering Techniques

Figure 5 shows that the MCL-ANFIS method fails to identify and unsegment drusen in locations where it blends in with the background or near a boundary. So, in order to make comparisons, MCL was used on the drusen. Thanks to the membership value assigned to each pixel by MCL, even the border-dwelling drusen could be accurately identified. MCL's more involved calculations ultimately provide more accurate classifications across the board. To account for less-defined pixels and quantify the degree of confidence (or error) in the final result, degrees of membership are used. However, as is the case with every ANFIS algorithm and its related seed, the final product is sub-optimal. Thus, in overlapping drusen and background regions, MCL clustering yields improved segmentation. The next step in quantifying the drusen is to construct a model from the clustered image. The size of a drusen is equal to the sum of all the pixels that have the same label. The sum of these areas tells us something about how a disease progresses as a whole. Drusen may be categorized as large, medium, or small based on their area (number of pixels), which is determined by their labelling. A photograph's drusen count may be used to assess age-related macular degeneration risk.

4.2 Performance Evaluation

Accurate segmentation is critical in medical image processing since it may impact the precisionof later phases, such as diagnosis and therapy. The quality of the color-segmented picture maybe evaluated in a number of ways, including qualitative ones. All subjective measurements must rely on human perception. Alas, the human visual system cannot be accurately represented by any objective criterion or quantitative formula. The quality of a segmentation result is dependent on a number of factors, such as whether or not it is homogeneous, spatially compact, continuous, and compatible with psycho-visual perception. Because of this, it is very unlikely that a single statistic could accurately represent all of these aspects. A good indicator of segmentation quality is the benefit it provides for a certain application. However, Sensitivity is used as a quantitative evaluation indicator because of its relevance to the proposed system. For each drusen quality, Figure 6 shows the clustered areaof the drusen region using ANFIS and MCL. The proposed MCL clustering method can accurately pinpoint the largest clusters.

Doi: https://doi.org/10.54216/FPA.150202
Received: July 20, 2023 Revised: November 19, 2023 Accepted: March 12, 2024

Figure 6: Area of Drusen Region Classified Under Each Grade

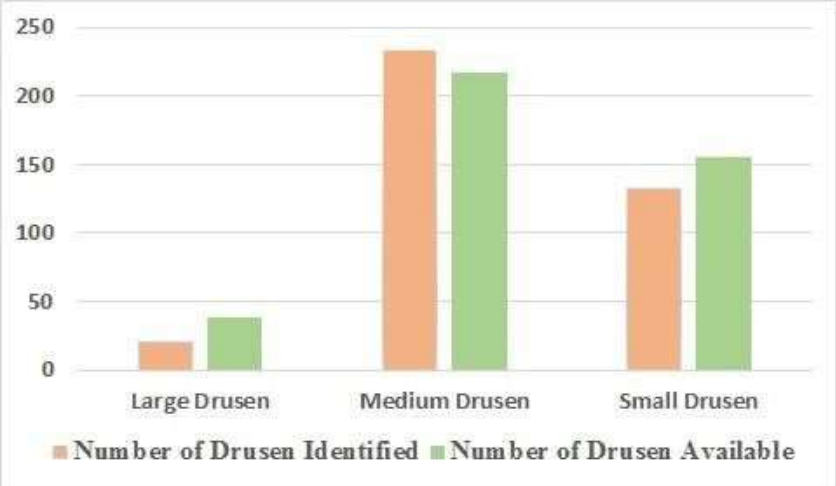

Figure 7: Counts of Individual Drusen

The quality of the first segmentation in medical image processing may have an impact on the efficacy of future phases like diagnosis and therapy. The color-segmented picture may be evaluated on a variety of qualitative scales. For every subjective evaluation, human perception is essential. However, the human visual system cannot be fully characterized by any objective criterion or quantitative formula. The quality of a segmentation result is dependent on its degree of homogeneity, spatial compactness, continuity, and compatibility with psycho-visual perception. Therefore, it's quite unlikely that a single metric could capture the whole complexity of the situation. The quality of a segmentation solution may be gauged in large part by how much value it contributes to a particular application. However, the suggested method relies heavily on Sensitivity, hence it is used as a quantitative evaluation metric. Each drusen quality's ANFIS and MCL-clustering is shown in Figure 8. The MCL clustering technique is recommended for reliably determining which clusters are the most important. The pictures were given to the experts, and any irregularities were pointed out to them. The information was converted to digital form for ease of use and comparison. Figure 7 shows the comparison of the total number of drusen detected in the ground truth photos to the total number of drusen identified in each grade. As shown in Fig. 8, the proposed method successfully identifies large drusen. In the realistic photo, large AMD can be noticed.

The number of really large drusen has reduced as a result of local consolidation of comparable drusen. Medium-stage AMD classification provides a similar difficulty. The suggested method has classified 233 AMD as medium, whereas the ground-truth pictures have only detected 217. There has been a rise in the prevalence of medium-sized AMD. Smudging leads to the misclassification of faint drusen with insignificant intensity variations from the background as medium drusen. Using the proposed method, we were able to get a FRR of 2% for large drusen, 2% for medium drusen, and 8% for small drusen, whereas we only got a FRR of 2% for ungraded drusen (Fig.8). This suggests that the vast majority of important drusen have been labelled. Precision, recall, and F-measure, three performance indicators calculated for drusen classification, are shown in Figure 8.

Doi: https://doi.org/10.54216/FPA.150202
Received: July 20, 2023 Revised: November 19, 2023 Accepted: March 12, 2024

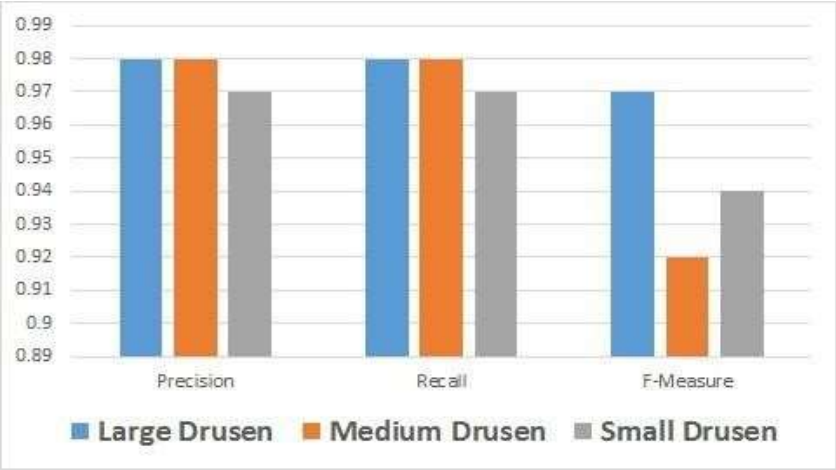

Figure 8: Performance Metrics of Drusen Segmentation Algorithm

Table 6: Comparison of performance metrics

CNN Models	Image Type	Data' set Sled	Accuracy	F1Score	F2 Score	Precision	Specifieity	Sensitivity
VGGil6 basedOscar	normal	SERI Dadaset	0.9375	.....	.....	-....	0.9375	0.9375
InceptionV3	normal	Kaggle	1.0	1.0	1.0	1.0	1.0	1.0
InceptionV3	Noisy image with σ = 0.002	Kaggle	0.875	0.66657	0.55556	1.0	1.0	0.5
Lnceptio nV/3	Noisy image with σ = 0.004	Kaggle	0.875	0.83333	0.66667	1.0	1.0	0.5
InceptionV3	Super resolution insage	Kaggle	1.0	1.0	1.0	1.0	1.0	1.0
InceptionV3	normal	Cellib ata Set	0.945	0.8579	0.8783	0.9045	0.9693	0.872
fnceptionV3	Noisy image with σ = 0.002	CelilData Set	0.826	0.6614	0.6724	0.6439	0.8746	0.6 s
InceptionV3	Noisy image with σ = 0.004	Cellib ata Set	0.7932	0.6087	0.6279	0.5791	0.844	0.6414
InceptionV3	Super resolat ion insage	CellData Set	0.953	0.9042	0.8944	0.9216	0.9746	0.888

Doi: https://doi.org/10.54216/FPA.150202
Received: July 20, 2023 Revised: November 19, 2023 Accepted: March 12, 2024

The quality of a segmentation result is dependent on its degree of homogeneity, spatial compactness, continuity, and compatibility with psycho-visual perception. Therefore, it's quite unlikely that a single metric could capture the whole complexity of the situation. The quality of a segmentation solution may be gauged in large part by how much value it contributes to a particular application. However, the suggested method relies heavily on Sensitivity; hence it is used as a quantitative evaluation metric. Each drusen quality's ANFIS and MCL-clustering is shown in Figure 8. The comparison of the proposed HEs detection method and a complete system for grading of DM is given below in Tables 8 and 9 respectively. With 100% sensitivity, 94.74% specificity, and 96% accuracy in distinguishing DM from non-DM pictures, the suggested technique displays very promising results. Table 7 provides the confusion matrix for your perusal. Figure 9 and Figure 10 show some sample pictures produced by the suggested method.

Table 7: Confusion matrix for detection of diabetic maculopathy

Total number of retinal images=150	Predicted (Non-DM)	Predicted (DM)	Total
Actual (Non-DM)	108 (TN)	06(FP)	114
Actual (DM)	0(FN)	36(TP)	36
Total	108	42	150

Table 8: Comparison of proposed method with existing techniques for HEs detection

Author	**Method**	**Sensitivity**	**Specificity**	**Accuracy**
AlirezaOsareh et al. [11]	Fuzzy C means clustering	92%	82%	-
Acharya U. et al. [23]	Higher order spectra	82%	88%	-
Proposed method	Color edge detection and mathematical morphology	**90%**	**92.72%**	**92%**

Table 9: Comparison of proposed method with existing techniques for grading of DM

Author	**Method**	**Database**	**Sensitivity**	**Specificity**	**Accuracy**
Lim et al. [24]	Marker controlled watershed transform	MESSIDOR	80.9%	90.25%	-
Proposed method	Mathematical morphology	MESSIDOR	**100%**	**94.74%**	**96%**

Based on the data in the table, it is clear that the suggested approach has sufficient reliability, efficacy, and efficiency to enter mainstream use, assisting medical professionals in the prevention, cure, or alleviation of diabetes symptoms, particularly retinal problems. Hard exudates are the bright lesions of the macula caused by extracellular yellow waxy lipid deposits. Blindness results from the inability of light to reach the retina due to the presence of hard exudates. Because of this, early diagnosis is crucial. Several different types of automated methods have been developed for locating deposits of exudates. These techniques often achieve an accuracy of 80%, seldom reaching 90%. This means you can't rely on them at all. A method that can reliably identify exudates automatically is the one based on edge detection and mathematical morphology. Its sensitivity is 90%, its specificity is 92.72%, and its accuracy is 92%.

Diabetic maculopathy may be graded thanks to the ability to identify exudates. For this reason, we recommend using a system based on mathematical morphology. The severity of diabetic macular edema is determined by how close exudate deposits are to the macula's central retina. Pre-processing, edge detection, exudates segmentation, blood vessels segmentation, undesirable bright object removal, and post-processing are the six

Doi: https://doi.org/10.54216/FPA.150202
Received: July 20, 2023 Revised: November 19, 2023 Accepted: March 12, 2024

basic phases that make up the grading of diabetic maculopathy. The suggested method's sensitivity (94.74%), specificity (94.74%), and accuracy (96.6%) are all high enough that it deserves serious consideration for usage by medical practitioners.

6. Conclusion

A poly-scale, dual-path CNN network was evaluated for its ability to distinguish between photos of AMD and Normal subjects. This network has a very low number of trainable parameters—just 0.7M. Finally, we have investigated classification frameworks for the identification of AMD at the picture level, using both CF images and OCT volumes. For the purpose of image-level identification of AMD in CF pictures, two techniques based on handmade features and deep learning, respectively, have been examined. Characteristics produced from the OD-OC segmentation and features derived directly from the area of interest surrounding the OD are used by both approaches in an effort to capture both the structural changes and the appearance. It has also been claimed that a 3D OCT volume may be used to diagnose AMD by modelling the structural changes in the Bruch's membrane as outliers relative to a normative OCT atlas. Therefore, the following is a synopsis of the results of this thesis. To jointly extract OD and OC borders from retinal CF pictures, a CRF framework has been developed. During testing, the approach models the OC border using just a single 2D CF picture to estimate depth. To identify the boundaries of numerous intraretinal layers in OCT images concurrently, we provide fully trained convolutional neural network (CRF) architecture. Both shape priors and appearance-based cost terms are included in the framework, and they are trained together in a Structural Support Vector Machine.

In order to simulate the level set-based curve evolutions inside the deep learning framework, a generic RNN Architecture has been developed for boundary-based segmentation. The approach shows promise for segmenting a variety of anatomical structures across disciplines. The methods for detecting AMD in CF and 3D OCT produce satisfactory results using computer-aided design software. Two approaches, one using deep learning and the other using handmade characteristics, have been investigated for AMD classification. Modeling the Bruch's membrane abnormalities caused by AMD as large departures from a Normative Atlas.

Funding: No external funding is received.

Conflicts of Interest: “The authors declare no conflict of interest.”

References

[1] Acharya, U.R., Hagiwara, Y., Deshpande, S.N., Suren, S., Koh, J.E.W., Oh, S.L., Arunkumar, N., Ciaccio, E.J. and Lim, C.M., 2019. Characterization of focal EEG signals: a review. Future Generation Computer Systems, 91, pp.290-299.

[2] Wan, Z., Yang, R., Huang, M., Zeng, N. and Liu, X., 2021. A review on transfer learning in EEG signal analysis. Neurocomputing, 421, pp.1-14.

[3] Khosla, A., Khandnor, P. and Chand, T., 2020. A comparative analysis of signal processing and classification methods for different applications based on EEG signals. Biocybernetics and Biomedical Engineering, 40(2), pp.649-690.

[4] SHu, L. and Zhang, Z. eds., 2019. EEG signal processing and feature extraction (pp. 1-437). Singapore: Springer.

[5] Hosseini, M.P., Hosseini, A. and Ahi, K., 2020. A review on machine learning for EEG signal processing in bioengineering. IEEE reviews in biomedical engineering, 14, pp.204-218.

[6] Jiang, X., Bian, G.B. and Tian, Z., 2019. Removal of artifacts from EEG signals: a review. Sensors, 19(5), p.987.

[7] Rahman, M.M., Sarkar, A.K., Hossain, M.A., Hossain, M.S., Islam, M.R., Hossain, M.B., Quinn, J.M. and Moni, M.A., 2021. Recognition of human emotions using EEG signals: A review. Computers in biology and medicine, 136, p.104696.

[8] Xie, Yu, and Stefan Oniga. "A Review of Processing Methods and Classification Algorithm for EEG Signal." Carpathian Journal of Electronic & Computer Engineering 12, no. 3 (2020).

[9] Stancin, I., Cifrek, M. and Jovic, A., 2021. A review of EEG signal features and their application in driver drowsiness detection systems. Sensors, 21(11), p.3786.

[10] Gao, Z., Dang, W., Wang, X., Hong, X., Hou, L., Ma, K. and Perc, M., 2021. Complex networks and deep learning for EEG signal analysis. Cognitive Neurodynamics, 15, pp.369-388.

[11] Xu, G., Shen, X., Chen, S., Zong, Y., Zhang, C., Yue, H., Liu, M., Chen, F. and Che, W., 2019. A deep transfer convolutional neural network framework for EEG signal classification. IEEE Access, 7, pp.112767-112776.

Doi: https://doi.org/10.54216/FPA.150202
Received: July 20, 2023 Revised: November 19, 2023 Accepted: March 12, 2024

[12] Siuly, S., Khare, S.K., Bajaj, V., Wang, H. and Zhang, Y., 2020. A computerized method for automatic detection of schizophrenia using EEG signals. IEEE Transactions on Neural Systems and Rehabilitation Engineering, 28(11), pp.2390-2400.
[13] Gao, Y., Gao, B., Chen, Q., Liu, J. and Zhang, Y., 2020. Deep convolutional neural network-based epileptic electroencephalogram (EEG) signal classification. Frontiers in neurology, 11, p.375.
[14] Merlin Praveena, D., Angelin Sarah, D. and Thomas George, S., 2022. Deep learning techniques for EEG signal applications–a review. IETE journal of Research, 68(4), pp.3030-3037.
[15] Chao, H., Dong, L., Liu, Y. and Lu, B., 2019. Emotion recognition from multiband EEG signals using CapsNet. Sensors, 19(9), p.2212
[16] Katmah, R., Al-Shargie, F., Tariq, U., Babiloni, F., Al-Mughairbi, F. and Al-Nashash, H., 2021. A review on mental stress assessment methods using EEG signals. Sensors, 21(15), p.5043.
[17] Saeidi, M., Karwowski, W., Farahani, F.V., Fiok, K., Taiar, R., Hancock, P.A. and Al-Juaid, A., 2021. Neural decoding of EEG signals with machine learning: A systematic review. Brain Sciences, 11(11), p.1525.
[18] Nagabushanam, P., Thomas George, S. and Radha, S., 2020. EEG signal classification using LSTM and improved neural network algorithms. Soft Computing, 24, pp.9981-10003.
[19] Venkatachalam, K., Devipriya, A., Maniraj, J., Sivaram, M., Ambikapathy, A. and Iraj, S.A., 2020. A Novel Method of motor imagery classification using eeg signal. Artificial intelligence in medicine, 103, p.101787.
[20] Yıldırım, Ö., Baloglu, U.B. and Acharya, U.R., 2020. A deep convolutional neural network model for automated identification of abnormal EEG signals. Neural Computing and Applications, 32, pp.15857-15868.
[21] Tsipouras, M.G., 2019. Spectral information of EEG signals with respect to epilepsy classification. EURASIP Journal on Advances in Signal Processing, 2019(1), pp.1-17.
[22][22]. Wang, J. and Wang, M., 2021. Review of the emotional feature extraction and classification using EEG signals. Cognitive robotics, 1, pp.29-40.
[23] Joshi, V.M. and Ghongade, R.B., 2022. IDEA: Intellect database for emotion analysis using EEG signal. Journal of King Saud University-Computer and Information Sciences, 34(7), pp.4433-4447.
[24] E.E. and Acharya, U.R., 2021. Automated ASD detection using hybrid deep lightweight features extracted from EEG signals. Computers in Biology and Medicine, 134, p.104548.
[25] Tawhid, M. N. A., Siuly, S., Wang, K., & Wang, H. (2023). Automatic and Efficient Framework for Identifying Multiple Neurological Disorders From EEG Signals. IEEE Transactions on Technology and Society, 4(1), 76-86.

Doi: https://doi.org/10.54216/FPA.150202
Received: July 20, 2023 Revised: November 19, 2023 Accepted: March 12, 2024